Title
Inhibitory Interactions and Columnar Inputs to an Object Motion Detector in Drosophila

Journal
Cell Reports, 30(7)

ISSN
2639-1856

Authors
Keleş, Mehmet F
Hardcastle, Ben J
Städele, Carola
et al.

Publication Date
2020-02-01

DOI
10.1016/j.celrep.2020.01.061

Peer reviewed

Published in final edited form as:

Cell Rep. 2020 February 18; 30(7): 2115–2124.e5. doi:10.1016/j.celrep.2020.01.061.

Inhibitory Interactions and Columnar Inputs to an Object Motion Detector in *Drosophila*

Mehmet F. Keleş[1,3], **Ben J. Hardcastle**[1,3], **Carola Städele**[1], **Qi Xiao**[1,2], **Mark A. Frye**[1,4,5,*]

[1]University of California, Los Angeles, Department of Integrative Biology and Physiology, 610 Charles Young Drive East, Los Angeles, CA 90095-7239, USA

[2]University of California, Los Angeles, Department of Biological Chemistry, Howard Hughes Medical Institute, David Geffen School of Medicine, Los Angeles, CA 90095, USA

[3]These authors contributed equally

[4]Present address: Johns Hopkins University, Department of Neurology, Baltimore, MD 21205, USA

[5]Lead Contact

SUMMARY

The direction-selective T4/T5 cells innervate optic-flow processing projection neurons in the lobula plate of the fly that mediate the visual control of locomotion. In the lobula, visual projection neurons coordinate complex behavioral responses to visual features, however, the input circuitry and computations that bestow their feature-detecting properties are less clear. Here, we study a highly specialized small object motion detector, LC11, and demonstrate that its responses are suppressed by local background motion. We show that LC11 expresses GABA-A receptors that serve to sculpt responses to small objects but are not responsible for the rejection of background motion. Instead, LC11 is innervated by columnar T2 and T3 neurons that are themselves highly sensitive to small static or moving objects, insensitive to wide-field motion and, unlike T4/T5, respond to both ON and OFF luminance steps.

Graphical Abstract

[*]Correspondence: frye@ucla.edu.

AUTHOR CONTRIBUTIONS

Funding Acquisition, M.A.F.; Conceptualization, M.A.F., M.F.K., and B.J.H.; Investigation, M.F.K., B.J.H., C.S., and Q.X.; Writing, M.F.K., B.J.H., and M.A.F.; Supervision, M.A.F.

SUPPLEMENTAL INFORMATION

Supplemental Information can be found online at https://doi.org/10.1016/j.celrep.2020.01.061.

DECLARATION OF INTERESTS

The authors declare no competing interests.

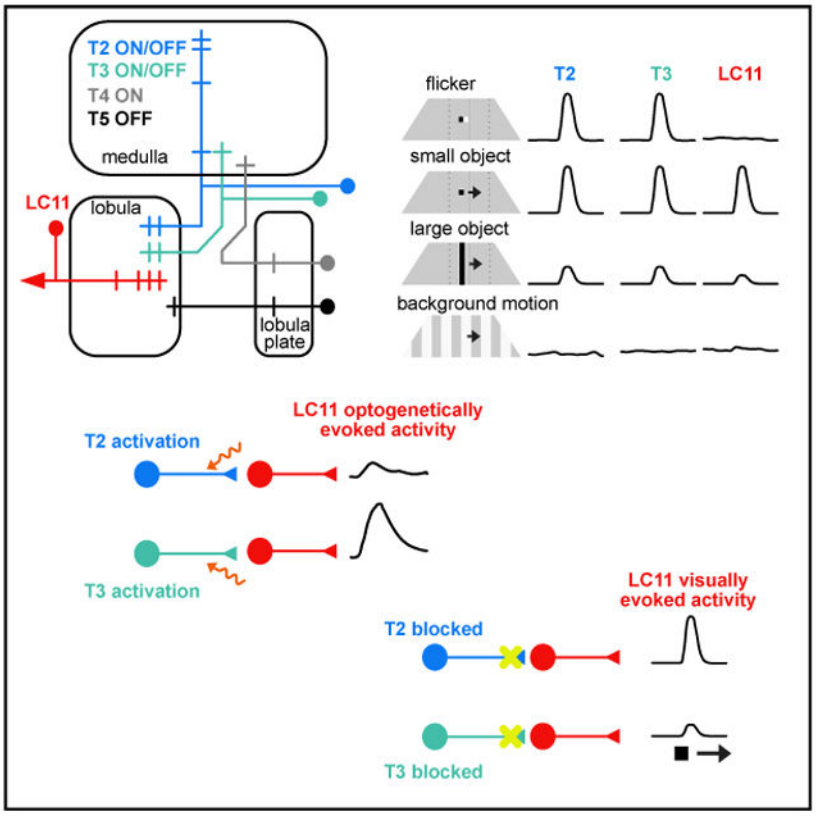

In Brief

Keleş et al. reveal the functional properties of two classes of small-field neurons that supply a highly specialized object detector. T2/T3 neurons are ON-OFF detectors of small visual stimuli, which interact through inhibitory receptors on their downstream targets to sculpt small-object selectivity and insensitivity to motion of the visual panorama.

INTRODUCTION

The cellular mechanisms of motion vision have become rapidly advanced owing to genetic, optogenetic, and *in vivo* imaging tools developed in *Drosophila melanogaster*. As in the mammalian retina, the fly optic lobe segregates ON and OFF polarity luminance changes into parallel cellular pathways. The ON- and OFF-selective pathways supply directionally selective columnar T4 and T5 neurons, respectively (Mauss et al., 2017). The terminals of these small-field retinotopic motion detectors innervate the third optic ganglion, the lobula plate, where their synaptic output is integrated within the large planar dendrites of projection neurons that map specific wide-field patterns of optic flow onto descending pre-motor neurons to coordinate visual behavior (Busch et al., 2018; Fisher et al., 2015; Maisak et al., 2013).

In parallel to the motion vision pathway of the lobula plate, projection neurons identified in the lobula have been shown to encode moving features such as edges or objects to influence complex visual behaviors (Ache et al., 2019; Aptekar et al., 2015; Keleş and Frye, 2017a,

2017b; von Reyn et al., 2017; Ribeiro et al., 2018; Wu et al., 2016; Zhang et al., 2013). Roughly 20 classes of lobula columnar neurons (LCs) project to the protocerebrum where axon terminals of each class form tight glomerular neuropils (Otsuna and Ito, 2006; Wu et al., 2016). Individual LC11 neurons as well as the glomerular ensemble are highly responsive to small contrasting objects moving in any direction across the ipsilateral field of view (Keleş and Frye, 2017a). Unlike the output cell types of the lobula plate, little is known about how the receptive field properties of LC11 arise. Here, we investigate the interactions between background motion and object responses in LC11, identify a role for GABA-mediated inhibition in shaping object detection by LC11, and identify presynaptic inputs to LC11. We show that columnar neurons T2 and T3 projecting from the medulla and terminating in the second and third layers of the lobula overlap with LC11 dendrites. We show that T2 and T3 synapse with dendrites of LC11, and T3 supplies excitatory input to LC11. Finally, we demonstrate that T2 and T3 neurons are highly selective for small objects, are suppressed by wide-field background motion, and unlike T4/T5, show full-wave rectified ON-OFF excitatory responses to rapid transitions in luminance.

RESULTS

The Onset of Background Motion Locally Suppresses Object Responses in LC11

We tested the hypothesis that LC11's response to a small, moving figure, which we refer to as an "object," persists as it moves against a the visual "background." We recorded visually evoked responses using two-photon GCaMP6m imaging (Figure 1A). We moved a dark object over a low contrast background grating. For object motion against a stationary background grating, LC11 responded with an increase in activity as the object entered the ipsilateral field of view (Figure 1B). The amplitude of this response was similar to that obtained for object motion over a uniform background (Keleş and Frye, 2017a). By contrast, object motion superposed against a grating moving in either direction reduced the average object response by ~93% (±3% SEM) (Figure 1C). We tested whether coherent background motion is needed to suppress LC11 object responses or if a flickering background can cause similar suppression. When each pixel in the background pattern flickered randomly at 10 Hz frame rate, LC11 responses to the moving object were reduced by ~88% (±4% SEM) (Figure 1D).

We then tested whether background suppression of LC11 is driven by a small-field spatial mechanism acting near the object path or instead by a wide-field mechanism. We presented the low contrast grating only in the contralateral quadrant of the display, a region outside of the ensemble receptive field of the LC11 optic glomerulus, and moved the dark object through the full azimuth of the display, as before. Under these conditions, object responses were unaffected by motion of the grating (Figure 1E). We then presented the grating only in the ipsilateral quadrant of the display, where the strongest responses to object motion are evoked. Motion of the grating in this position did not appear to affect LC11 responses until the object overlapped with the moving grating, at which point responses were strongly reduced (Figure 1F). We explored the temporal dynamics of this interaction by transitioning from a stationary background to a moving one while the object passed across the display. When we delayed the onset of grating motion until LC11's response to the object had

already peaked, LC11 responses were immediately and continually suppressed (epoch 1 versus epoch 4) (Figure 1G).

We next tested how extensive and how close to the object's path local background motion must be in order to suppress object responses. We moved the object on the same central azimuthal path as before and constricted the moving grating from the top and bottom of the display, thereby reducing the gap through which the object swept. Reducing the gap systematically attenuated the object response down to a threshold of roughly 30°: for smaller gap sizes the 8.8° object failed to elicit responses in LC11 (Figures 1H and 1I). It is noteworthy that the vertical receptive field size of individual LC11 neurons is ~20° (Keleş and Frye, 2017a). Taken together, our results demonstrate that either coherent motion or flicker suppresses object responses in LC11, and these destructive cues act in a spatially localized manner, within a distance equivalent to a single LC11 receptive field. We next investigated how this suppression is mediated at a molecular level.

LC11 Expresses Acetylcholine and GABA Receptors

Previous work has shown that LC11's preference for small object motion is eliminated by bath application at low concentration of the GABA-blocker picrotoxin (PTX): responses to wide-field grating motion and to an elongated bar were "released" by PTX as expected by the prediction that inhibition filters global motion cues from object detectors (Keleş and Frye, 2017a). However, responses to a small contrasting object were unexpectedly attenuated, suggesting that GABAergic inhibition plays a role in LC11's responses to object motion. LC11 dendrites primarily innervate layers 2/3 of the lobula, in addition to layers 4/5 where they express presynaptic markers. Layers 2/3 are heavily enriched for the vesicular GABA transporter (VGAT) (Keleş and Frye, 2017a) so LC11 dendrites could receive GABAergic inhibition here. To test whether LC11 expresses an inhibitory GABA receptor, we used a recently generated T2A-Gal4 insertion into the GABA-A receptor subunit *Rdl* (Diao et al., 2015). This allowed expression of Gal4 in the same pattern as the native *Rdl*. We then labeled putative *Rdl*-expressing cells with a membrane tagged version of tdTomato, while driving the expression of GFP using an LC11-LexA driver (Figure S1A). We found co-labeling of GFP with RFP in cell bodies (Figure S1A), suggesting that LC11 expresses *Rdl*. Using the same strategy, we found that LC11 transcribes the nicotinic acetylcholine receptor subunits α1, α6, and α7 but not subunit α5 (Figure S1B), suggesting that LC11 receives cholinergic excitation. We then tested whether LC11 itself synthesizes the inhibitory neurotransmitter GABA, which could mediate feedback inhibition directly via its own GABA receptors. However, we found that LC11 cell bodies do not co-label with the GABA antibody (Figure S1C). To directly test whether LC11 could nevertheless contribute feedback inhibition to columnar neighbors, we co-expressed the temperature sensitive synaptic blocker shibire^{ts1} with GCaMP6f. Blocking synaptic output had no influence over the selective filtering of bar and wide-field grating stimuli by LC11 (Figure S1D). Finally, co-labeling experiments against the vesicular glutamate transporter revealed that LC11 is not glutamatergic (Figure S1E) but rather is positive for ChAT (Figure S1E).

Object Responses in LC11 Are Enhanced by GABAergic Inhibition

To explore how GABAergic input to LC11 might sculpt object selectivity, we used the FlpStop technique (Fisher et al., 2017) to specifically disrupt *Rdl* subunit expression in LC11 and investigate how a lack of GABA-A receptors affected object and background motion responses. Eliminating *Rdl* expression in LC11 led to a reduction of responses to small objects by ~40% in comparison to controls lacking the FLP expression (Figure 2A). Responses to an elongated bar and wide-field grating motion were not affected by *Rdl* knockout (Figures 2B and 2C). Curiously, responses to the motion of a bright object doubled on average compared to controls (Figure 2D). Knocking out *Rdl* had no effect on responses to larger visual stimuli such as objects moving on a flickering background or a looming object (Figures 2E and 2F), which together indicates that none of the wide-field filtering exhibited by LC11 occurs via direct presynaptic inhibition. A unique characteristic of LC11 is its relative insensitivity to light increments/decrements alone: LC11 is selective for object motion rather than local flicker. We found that *Rdl* does not modulate LC11's insensitivity to flickering objects (Figure 2G). To verify that *Rdl* was conditionally disrupted as expected, we exploited the fact that the flipping event brings a tdTomato sequence into proximity with a UAS sequence, allowing cell-autonomous labeling of cells that underwent successful inversion using FlpStop. We found strong overlap between GCaMP6f and cytosolic tdTomato in LC11 cell bodies (Figure 2H), confirming the successful knockout of *Rdl*. Together these results indicate that LC11 relies on postsynaptic GABA signaling to sculpt its response properties for small object motion including its preference for contrast polarity, which helps to explain why LC11 responses to small objects essentially disappear in the presence of bath-applied picrotoxin (PTX) (Keleş and Frye, 2017a). Unlike with the bath application of PTX, responses to wide-field stimuli motion did not increase with *Rdl* knockout (Figures 2C-2F), suggesting that the rejection of wide-field motion cues does not occur via postsynaptic inhibition of LC11.

T2 and T3 Neurons Innervate LC11 Dendrites

Recent connectome efforts have identified numerous cell types that participate in fly motion vision (Shinomiya et al., 2014, 2019; Strother et al., 2017; Takemura et al., 2013, 2017). We examined four *trans*-medullary cell types that innervate the outer layers of the lobula in the vicinity of LC11 dendrites: Tm2, Tm4, and Tm9 in the OFF-motion pathway and Tm3 in the ON pathway (Figure S2). Double labeling shows no overlap of Tm2 and Tm9 with LC11, and slight overlap of Tm3 and Tm4 with LC11 in layer 3 (Figure S2). However, the dense dendritic field of LC11 housed within the medial portion of layer 2 does not overlap with any of the Tm cells tested leading us to conclude that the majority of inputs to LC11 are not directly dependent upon columnar inputs to the T4/T5 motion pathway.

To identify presynaptic inputs to LC11, we performed an unbiased computational screen using the publicly available Janelia Gal4 database (see STAR Methods) (Jenett et al., 2012). This led to the identification of ~100 lines that label cells in the optic lobe that putatively overlap with LC11 dendrites. To confirm the overlap, we tested Gal4 lines through double labeling, with GFP expressed in LC11 and RFP expressed in each of the candidate input lines. From this screen, we identified Gal4 lines that labeled the columnar neurons T2 and T3, identified by their dendritic and axonal layer specificity in the medulla and lobula,

respectively (Figures 3A and 3B) and cell bodies located between the posterior rim of the medulla and the lobula plate (Fischbach and Dittrich, 1989). T2 dendrites heavily innervate medulla layers 1, 2, and 9 whereas T3 dendrites innervate layer 9. In the lobula, the terminals of T2 are located in layers 2 and 3 the terminals of T3 are found in layer 3 (Figure 3F). To assess synaptic connectivity between T2/T3 and LC11, we used the anterograde transsynaptic circuit tracing system *trans*-Tango (Talay et al., 2017) to express tdTomato in neurons postsynaptic to any cell type in the candidate Gal4 lines. Both T2 > *trans*-Tango and T3 > *trans*-Tango showed outputs in the LC11 glomerulus, which is readily identifiable by its unique anatomical profile among other LC optic glomeruli (Figures 3C-3E and S3). We generated split-Gal4 lines for both T2 and T3 using publicly available hemidrivers (Dionne et al., 2018; Tirian and Dickson, 2017) and confirmed cellular identity with stochastic single-cell labeling Multi Color FlipOut (MCFO) (Nern et al., 2015) (Figure S4). Within the T2 line, we also found single-cell clones of the distinctive T2a neuron (2 out of 46 clones, Figure S4B′), which primarily innervates distal part of M3 and does not exhibit extensive bushy dendrites compared to T2 dendrites located in M2. These anatomical results indicate that T2 and T3 neurons are both strong candidates to supply visual input to LC11 object detecting neurons.

T2 and T3 Are Highly Sensitive to Small Objects

We next characterized the basic physiological response properties of T2 and T3 using two-photon calcium imaging. We imaged from small regions of interest (ROIs) in the lobula (Figure 3G). As with LC11, we found that T2 and T3 both respond strongly to a small moving object, show an intermediate response to a bar, and almost no response to wide-field grating motion (Figure 3H). Because the columnar T2 and T3 neurons are developmentally related to the motion detecting neurons, T4 and T5 (Apitz and Salecker, 2018), and share some of the same synaptic inputs from the medulla (Shinomiya et al., 2019; Takemura et al., 2015), we made direct comparisons among all four cell types. One of the most salient properties of T4 and T5 is ON and OFF selectivity, respectively. Thus, we first explored T2/T3 responses to small ON/OFF flash stimuli. We varied the intensity of a stationary 8.8 × 8.8° object, presented against a mid-level intensity uniform background, in steps lasting 500 ms (Figure 4A). T2 responded with a complex waveform that indicated excitation to both the OFF and ON phases of the flash sequence, with decaying responses to the interspersed background intensity. By contrast, T3 showed a cascade of excitatory responses to any luminance change, regardless of its polarity (Figure 4A). Thus, T2/T3 flash responses did not demonstrate ON/OFF polarity segregation, standing in stark contrast to T4/T5 responses (Figure 4A).

We then tested a battery of motion stimuli that elicit known responses in LC11 including an 8.8 × 8.8° small object, a single-edge horizontally elongating object, an 8.8 × 70° vertical bar, and the same bar elongating horizontally. We presented these stimuli both darker-than-background and brighter-than-background. We also presented a horizontally drifting wide-field vertical grating with a period of 17.6°. A summary of normalized maximum responses for each cell type to each stimulus moving front-to-back motion is displayed in Figure 4B (results were qualitatively similar for other cardinal directions, not shown).

Across all stimuli, T2 cells generally responded most strongly to the small bright object, and T3 cells responded most strongly to the small dark object (Figure 4B). However, by contrast to T4/T5, T2 and T3 preferences for ON or OFF polarity edge stimuli were weak and (Figure 4B). Notably, whereas T2 appeared to be broadly indifferent to the presence or absence of a trailing-edge, T3 responded more strongly to the OFF-ON or ON-OFF sequence produced as a small object moved through its receptive field, compared to the equivalently sized OFF-only edge (50% less than dark object response, $p = 0.0004$) or ON-only edge (59% less than dark object response, $p = 0.002$).

T4/T5 neurons are known to show size-tuning mediated by lateral inhibition (Fisher et al., 2015). Similarly, both T2 and T3 showed considerably smaller responses to elongated bars and edges than to small objects, and nearly zero response to wide-field gratings, demonstrating an even greater suppression of wide-field stimuli than T4/T5 (Figure 4B). The selectivity of T2 and T3 to figures of small vertical size and, in the case of T3, small horizontal size, and their contrast polarity-indifference broadly match the response properties of LC11 (Keleş and Frye, 2017a), suggesting that LC11 inherits these properties from T2/T3.

T3 Provides Functional Excitatory Input to LC11

The anatomical projections (Figures 3A and 3B), transsynaptic label (Figures 3C-3E), and response properties of T2 and T3 (Figures 3H, 4A, and 4B) suggest that the output of these cells are largely responsible for the visual receptive field properties of LC11 neurons. To test whether T2 or T3 activity is sufficient to excite LC11, we expressed the red-shifted channelrhodopsin, Chrimson in T2, T3, and T4/T5 neurons under the control of split-Gal4 drivers (Figure S4), and GCaMP6s in LC11 neurons. We recorded activity within the LC11 glomerulus in response to excitation of Chrimson by a 625 nm LED placed externally near the animal's head. Chrimson excitation of a promoterless "empty" split-Gal4 construct did not evoke measurable GCaMP6s responses in LC11 (Figure 4C). LC11 responses were elevated but not significantly for Chrimson excitation of T2 neurons (Figure 4C). By contrast, excitation of T3 cells evoked a large response in LC11 (Figure 4C). To illustrate the specificity of action of T3 onto LC11, we performed a control in which we expressed Chrimson in T4/T5 neurons, the latter of which has dendrites within the outer layers of the lobula (Fischbach and Dittrich, 1989). As expected, Chrimson excitation of T4/T5 failed to excite LC11 (Figure 4C), but in some preparations caused GCaMP6s fluorescence in LC11 several seconds after Chrimson was switched off. These results suggest that population excitation of T3, but not T2, is sufficient to elicit calcium transients in LC11 terminals.

To explore whether T2 or T3 activity is necessary for LC11 responses to visual stimuli, we blocked their chemical synaptic output using shibire^{ts1} and recorded visually evoked GCaMP6f activity in LC11 (Figure 4D). Across a range of speeds, LC11's peak response to a small dark object occurred at 220°/s in genetic control animals. LC11 activity was significantly reduced at the same speed for animals in which shibire^{ts1} was expressed in T3 neurons. Responses at two lower speeds were also affected. For a small bright object, LC11's peak response occurred at 110°/s in control animals and this was reduced when the output of T3 was blocked. For both the bright and the dark object, there was no significant

impact on the amplitude of LC11's activity when the output of T2 was blocked. To explore whether LC11's size-tuning was affected by blocking T2 or T3 output, we varied the vertical size of a dark object with 8.8° width at the center of the display (Figure 4D). As expected, in control animals we observed preferential responses in LC11 for the smallest, 8.8 × 8.8°object, which decreased as the object was elongated vertically. When the output of T3 was blocked, we observed a reduction in LC11's response to the 10° object but no significant effect for larger sizes, preserving the preference for the smallest object. Again, there was no change in the amplitude of LC11 responses across the range of sizes tested when the output of T2 was blocked (Figure 4D). Taken together, these functional results suggest that T3 is sufficient to elicit excitatory responses in LC11 and necessary for proper visually evoked responses in LC11.

DISCUSSION

Emergence of Object Detection from Flicker-Sensitive Inputs

In vertebrates, neurons in the retina partially encode object information, but fail to discriminate flicker from coherent motion (Kim and Kerschensteiner, 2017; Kim et al., 2015; Zhang et al., 2012). Yet, higher-order neurons in the mouse superior colliculus respond strongly only to moving stimuli (Bennett et al., 2019; Gale and Murphy, 2016). Similarly, we found that T2/T3 neurons are selective for small objects (Figure 4B), but respond to ON and OFF flicker as well, whereas downstream LC11 is responsive to object motion, not stationary flicker (Keleş and Frye, 2017a). We propose that LC11 computes continuous object motion from local ON-OFF transients conveyed by T2/T3. Future work on examining the spatiotemporal patterning of columnar inputs to LC11, as well as the cognate neurotransmitters and receptors should reveal how these computations are achieved.

Role of Inhibition in Sculpting LC11 Object Selectivity

In prior work (Keleş and Frye, 2017a), we demonstrated that bath applied PTX, which selectively blocks chloride currents carried by GABA-A channels or glutamate channels (Zhang et al., 1995), resulted in LC11 displaying uncharacteristic responses to elongated bars and gratings. This result was predicted under the presumption that inhibition actively filtered wide-field input from LC11. Curiously, in the same preparation, the small object responses for LC11 were essentially eradicated. How can global loss of inhibition by bath applied PTX explain both enhanced wide-field responses and diminished small object responses in LC11? Several lines of evidence suggest that postsynaptic inhibitory neuromodulation acts on LC11 in a center-surround fashion. LC11 expresses both acetylcholine receptors and a GABA-gated chloride channel subunit *Rdl* (Figures S1A and S1B). Blocking GABA-A mediated synaptic currents by genetic disruption of *Rdl* specifically in LC11 neurons results in a decrease in response amplitude to the smallest object we tested, and yet, importantly, had no effect on the normal attenuated responses to bars or normal absence of wide-field grating responses (Figure 2). Our results support a working model in which *Rdl* knockout unmasks an ON-pathway input while decreasing the normal OFF object response of LC11 (Figure 2D). These properties could be explained by an ON-pathway GABAergic input to LC11 through *Rdl* that normally occludes ON excitation and disinhibits OFF responses. The corollary is that suppression of responses to

large objects or wide-field motion occurs upstream of these object detectors. Indeed, LC11 appears to inherit its sensitivity to small object motion from excitatory T2/T3 inputs, perhaps themselves having surround inhibition mechanisms similar to T4/T5 (Fisher et al., 2015). There appears to be two mechanisms of action that are disrupted by PTX application on LC11 receptive field properties (Keleş and Frye, 2017a): crossover inhibition in T2/T3, which would explain their size-tuning, and local inhibition on LC11 that normally enhances small object responses. Thus, we propose that upon PTX delivery abnormal bar and wide-field motion responses are conveyed from T2/T3 to LC11 and small object responses are no longer boosted.

The importance of dynamic, stimulus-specific inhibition for spatial vision has been elucidated by other studies. In mice, cortical V1 center-surround receptive fields reveal stronger inhibitory currents than excitatory currents in both the surround and center, while inhibitory currents are spread more laterally than excitatory currents (Haider et al., 2013). In a visual collision detection circuit in the locust, feedforward inhibitory neurons actively encode dynamical variables such as object angular size (Wang et al., 2018). The inhibitory GABA-A receptor subunit *Rdl* is expressed by nearly all neurons of the fly visual system so far tested (Davis et al., 2018), highlighting the ubiquity and importance of inhibition for spatial vision.

T2 and T3 Neurons Are Size-Tuned and Selective for the Features that Excite LC11

T2 and T3 neurons share several key features with LC11. First, both show significantly larger responses to small solid objects than to single object edges or elongated bars, with virtually no response to moving wide-field gratings (Figure 4B). In the large calliphorid fly *Phaenicia sericata*, T2 neurons have been examined with intracellular sharp electrodes (Douglass and Strausfeld, 2003), which showed that these columnar neurons depolarize to the OFF-phase of flicker, and hyperpolarize to the ON-phase. This contrasts to our GCaMP6f recordings in *Drosophila*, in which T2 is excited by both ON and OFF luminance transitions (Figure 4B). Additionally, in *Phaenicia* T2 responded robustly to 80 × 62° moving gratings, whereas in *Drosophila* we observed no response in either T2 or T3 to gratings that filled our 108 × 63° display. The T2a cell type, with similar anatomy but different presynaptic inputs to T2 (Takemura et al., 2015), may show responses more closely matching those from larger flies.

An important feature of *Drosophila* T2/T3 neurons is that unlike T4 and T5 columnar motion detectors, which act as half-wave rectifiers that segregate ON and OFF edge stimuli, respectively (Figure 4B) (Maisak et al., 2013), both T2 and T3 neurons show full-wave rectification in that they are excited by both ON and OFF phases of flicker (Figure 4A). Notably, T5 shows similar amplitude responses to the OFF edges generated by either a solid two-edged dark object or a single moving OFF edge, whereas T3 responses are markedly stronger for the solid object presenting an OFF-ON sequence than to a single progressing OFF edge (Figure 4B). T3 appears to receive input from a combination of neurons that reside in the ON and OFF pathways, including Mi1 and Tm3 (Takemura et al., 2015), providing a possible explanation for this result. Full-wave rectification of ON and OFF stimuli is consistent with single point correlation computations proposed to comprise

elementary small target motion detectors (ESTMDs), which underlie the high performance object detection seen in lobula wide-field STMD neurons of hoverflies and dragonflies (Wiederman et al., 2008, 2013). Future work must explore the mechanisms that shape responses in T2 and T3, and how the spatiotemporal patterns of input from T2 and T3 confer discrimination of object motion from flicker in LC11.

STAR★METHODS

LEAD CONTACT AND MATERIALS AVAILABILITY

Further information and requests for resources and reagents should be directed to and will be fulfilled by the Lead Contact, Mark Frye (frye@ucla.edu).

All unique/stable reagents generated in this study are available from the Lead Contact without restriction.

EXPERIMENTAL MODEL AND SUBJECT DETAILS

Expression systems—To drive expression of transgenes in targeted tissues, Gal4/UAS (Brand and Perrimon, 1993), LexA/LexAop (Lai and Lee, 2006) and Split-Gal4/UAS (Luan et al., 2006) expression systems were used. Complete genotypes for each figure are in Table S1.

Calcium Imaging Experiments—Flies were raised on standard cornmeal/molasses food at 25°C and kept under a 12-hour light/ 12-hour dark cycle. 12-17 day old female flies used for RDL-FLPSTOP (Figure 2) experiments and 3-7 day old female flies used for all other experiments. For Chrimson activation experiments, control and experimental flies were transferred to food with 0.5mM all-trans-retinal (Sigma Aldrich, R2500) for at least 3 days on a 24-hour dark cycle.

Mapping synaptic connectivity with trans-Tango—Flies were reared on standard cornmeal medium and kept at 18°C under 12-hour light/12-hour dark cycle. 18-21 day old female adult flies used for confocal imaging.

Anatomical connectivity experiments—All experiments were performed on 3-7 day old female flies reared on standard cornmeal molasses food at 25°C kept under 12-hour light/12-hour dark cycle.

METHOD DETAILS

Anatomical Overlap—To find candidate lines that showed expression in the lobula layers where LC11 dendrites are located, we first downloaded ~3500 registered stacks of Janelia-Gal4 lines (Jenett et al., 2012) using R package vfbr (https://rdrr.io/github/jefferis/vfbr/man/download_gmr_stacks.html). Fiji plugin simple neurite tracer was used to label LC11 dendrites in the registered stacks, and a 3D voxel encompassing the dendrites created using the LC11-Gal4 stack. A custom written MATLAB script was used to create a binary mask from the 3D voxel. GFP labeling in the binary mask was then quantified across all registered stacks using MATLAB. We then visually inspected 400-500 lines that showed the highest

expression. Roughly 100 lines were selected for a dissection screen to label and visualize the candidate lines with overlapping expression within the dendritic domain of LC11. Driver lines with sparse optic lobe labeling were preferred.

Driver Lines and Generation of Split-Gal4s—For LC11 we used three LexA drivers interchangeably (see Key Resources Table). Two of the driver lines (R20G06 and R51F09) showed labeling in LC21, which forms a neighboring glomerulus to LC11. LC21 has distinct receptive field properties and does not exhibit strong responses to small objects (data not shown). Thus, in our experiments, we were able to confirm the LC11 glomeruli successfully.

To generate split-Gal4 lines we first checked the expression pattern of the candidate lines by crossing them to UAS-GFP. This suggested that R47E02 (Figure S4D) and VT012791 (Figure 3A) likely labels T2 due to strong labeling in distal medulla layers, whereas VT008463 (Figure S4E) and VT002055 (Figure 3B) likely labels T3. In addition, we identified a line (R65B04) that labels both T2 and T3 (data not shown). We then confirmed the cellular identity of these lines using MCFO. This confirmed that R47E02, VT012791 and R65B04 label T2, whereas VT002055, VT008463 and R65B04 label T3. Finally, we made lines that carry different combinations of AD and DBD hemidrivers for these lines. This resulted in T2-spGal4 and T3-spGal4 (see Key Resources Table and Table S1). It is important to note that the expression levels of split-Gal4s are often lower than the full drivers that they are derived from. The experiments involving activation or blocking of neurons to test connectivity can be sensitive to such changes. Our experiments with T3-spGal4 yielded positive results indicating that T3 is functionally connected to LC11, yet we observed an insignificant but trending signal in LC11 when T2 is activated. Thus, it is possible that a stronger spGal4 for T2 might be required to reliably test connectivity with LC11.

Two-photon calcium imaging—Two-photon calcium imaging was performed as previously described (Keleş and Frye, 2017a). Briefly, a female fly was cold anesthetized and placed on a hole that was etched on a steel shim, which was glued to a 3D printed holder. Designs of the holder and the dimensions of the shim were modified from Weir and Dickinson (2015). The fly was gently pushed so that the thorax protruded through the opening in the shim but the abdomen remained below. The position of the head capsule was adjusted using blunt forceps and the posterior surface of the head tilted roughly parallel to the long body axis. The head capsule and thorax were glued using UV-curable glue (#44600, Fotoplast Gel, Dreve). The legs and proboscis were fixed with beeswax. A small opening was made using fine forceps (#5SF, Dumont) on top of the target region. Fat and muscle #1 were removed to gain optical access to the imaging site of the optic lobe. The brain was bathed in saline (103mM NaCl, 3mM KCl, 1.5mM $CaCl_2$, 4mM $MgCl_2$, 26mM $NaHCO_3$, 1mM NaH_2PO_4, 10mM trehalose, 10mM glucose, 5mM TES, 2mM sucrose) and continuously perfused at 1-2 ml/min. The temperature of the bath was kept at 21°C by an inline solution heater/cooler (SC-20, Warner Instruments) connected to a temperature controller (TC-324, Warner Instruments). GCaMP was imaged at 920 nm using a Ti:Sapphire pulse laser (Coherent, Santa Clara, CA) controlled by Slide-Book (3i, Boulder,

CO). Images were acquired at 10-18 Hz. Flies were preincubated at 37°C for an hour and imaged at 20°C for the experiments utilizing *shibire*^{ts1}. To deplete available vesicles, a visual stimulus consisting of a small object moving across all parts of the display was presented three times preceding the experiment. Imaging time did not exceed 20 minutes.

Single plane images of LC11 terminals located in the ventrolateral protocerebrum were recorded for experiments involving LC11. The terminals were chosen for ease of access and bulk signal from all LC11s. We have previously shown that terminal recordings largely overlap with cell body and dendrite responses (Keleş and Frye, 2017a). For T2 and T3, terminals in the lobula were recorded. For T4 and T5, dendrites in the medulla and lobula were recorded, respectively.

Visual Display and Visual Stimuli—An arena composed of 48 8x8 LED panels (470 nm, Adafruit) were used to deliver visual stimuli. Three layers of blue filter (Rosco, no 59. Indigo) were placed onto the panels to prevent light leaking into the photomultiplier tubes. The LED display covered ± 108° in the horizontal axis and ± 32° in the vertical axis. Each pixel corresponded to 2.2° coverage on the retina at the eye's equator. There was a slight variation in pixel size in the elevation projection due to the difference between the curvature of the eye and the vertically flat display, but the distortion was equivalent to less than one optical pixel. The presentation orders for all stimuli were randomized and a 4 s blank display was interspersed to prevent adaptation. Each experimental condition was repeated 3-4 times.

In Figure 1B an 8.8°x8.8° dark (0% of maximum intensity) object was moved at 22°/s on a square-wave grating background of bright (15% of maximum intensity) and dark (69% of maximum intensity) bars with a period of 35.2°. In Figure 1C, the background was moved at 22°/s in both anterior-to-posterior and posterior-to-anterior directions. The same stimulus was used in Figure 1G, but the onset of the background movement was delayed 6.7 s, equivalent to the amount of time for the object to enter the receptive field of LC11.

In Figures 1D and 2E an 8.8°x8.8° dark (0% of maximum intensity) object was moved at 22°/s on a background with randomly distributed bright (15% of maximum intensity) and dark (69% of maximum intensity) pixels, of equal number. The background was either stationary or updated from a pool of 96 random backgrounds at 10 Hz.

In Figures 1E and 1F, an 8.8°x8.8° dark (0% of maximum intensity) object was moved at 22°/s on a background that consisted of a square-wave grating patch of bright (15% of maximum intensity) and dark (69% of maximum intensity) bars with a period of 17.6°. The square-wave grating patch extended 70.4° in the horizontal axis and 70.4° in the vertical axis and located either on the contralateral (Figure 1E) or ipsilateral (Figure 1F) side. The grating within the patch was moved at 22°/s in both anterior-to-posterior and posterior-to-anterior directions.

In Figure 1H an 8.8°x8.8° dark(0% of maximum intensity) object was moved at 22°/s on a square-wave background of bright (15% of maximum intensity) and dark (69% of maximum intensity) bars that varied in the vertical axis as indicated in the figure with a period of 35.2°.

The object moved in both anterior-to-posterior (shown) and posterior-to-anterior directions (not shown) while the square-wave grating patch moved at 22°/s in the opposite direction.

In Figures 2-2D an 8.8°x4.4° and 8.8°x70.4° dark object (0% of maximum intensity) was moved at 55°/s on a uniform bright (46% of maximum intensity) background in anterior-to-posterior direction. A square-wave grating of bright (46% of maximum intensity) and dark (0% of maximum intensity) bars with a period of 35.2° moved at 35.2°/s. A bright (46% of maximum intensity) 8.8° square object moved at 55°/s in anterior-to-posterior direction on a uniform dark (0% of maximum intensity) background.

In Figure 2F a dark (0% of maximum intensity) spot size of 2.2° appeared on a uniform bright (46% of maximum intensity) background and expanded reaching 61.6° in diameter. Speed of the loom was 550 ms and determined by the ratio of its radius to the velocity (r/v).

In Figure 2G an 8.8°x8.8° dark (0% of maximum intensity) or a bright (92% of maximum intensity) object was appeared for 4 s and disappeared on a uniform bright (46% of maximum intensity) background.

In Figure 3G an 8.8°x8.8° and 8.8°x70.4° dark (0% of maximum brightness) object was moved at 39.6°/s on a bright background (33% of maximum brightness). A square-wave grating composed of bright (60% of maximum brightness) and dark (13% of maximum brightness) bars with a period of 17.6° moved at 39.6°/s.

For T cell recordings in Figure 4A, an 8.8°x8.8° static object was presented randomly at 64 locations covering the ipsilateral visual field. In each presentation the object was initially the same brightness (33% of maximum) as the background. An initial OFF step decreased the brightness of the object (0% of maximum) for 0.5 s before returning to the background brightness for 0.5 s. An ON step then increased the brightness of the object (67% of maximum brightness) for 0.5 s before returning to the background brightness. In Figure 4B the 8.8°x8.8° bright (67% of maximum brightness) and dark (0% of maximum brightness) objects were moved along 8 trajectories of differing elevation along the azimuth at 39.6°/s on an intermediate background (33% of maximum brightness). The same brightness, background and speed were used for the bright and dark 70.4°x8.8° bars, presented at a single elevation. For experiments that presented an expanding edge, the same brightness and background were used as for the objects and bars. The leading edge moved at 36.3°/s. A square-wave grating as used for Figure 3G moved at 39.6°/s. Each stimulus duration was 2 s. The display was turned off for 1 s between each stimulus presentation.

For recordings in LC11 in Figure 4D, bright and dark small objects and a dark bar, each with brightness as in Figure 4B on the same brightness background, were presented moving from 0° in front of the fly at 110°/s toward the back of the fly on the ipsilateral side. A square-wave grating as used for Figure 3G moved at 110°/s in the contralateral to ipsilateral direction.

Optogenetic stimulation—Experimental and control flies were raised on food with all-trans-retinal, as described above. Calcium imaging was performed in the LC11 glomerulus, as described above, with a 625 nm LED (Thorlabs) positioned as close to the fly's head as

possible, illuminating the entire eye ipsilateral to the recording site for 1 s every 60 s, repeated at least three times. The intensity of the light falling on the surface of the eye was measured as 10.6 mW/cm^2. Between trials, a small dark object stimulus, as used for Figure 4B, was presented and used to confirm normal visual responses in LC11 and guide ROI selection.

Immunofluorescence Labeling—3 to 7 day old female flies were dissected in PBS using fine forceps (#5 Dumont). Dissection time never exceeded 20 minutes. Dissected brains were placed in 4% PFA and fixed for 25 minutes at RT, followed by washing with PBST (0.3% v/v Triton X-100) 3 times for 15 minutes each. Brains were than incubated in PBST-NGT (5% normal goat serum in PBST) for 30 minutes at RT and then in primary antibodies for 2 days at 4°C in PBST-NGT. This was followed by 3 washes for 15 minutes in PBST at RT. Brains were then placed in secondary antibody in PBST-NGT and incubated 2 days at 4°C. After washing several times with PBST, brains were mounted on a microscope slide in Vectashield (H-1000). The following concentrations are used for primary and secondary antibodies: Figures 2F and S1: chicken anti-GFP (1:1000, abcam, 13970), rabbit anti-DsRed (1:200, Takara, 632496), goat anti-chicken, Alexa Fluor 488 (1:1000, abcam, 150169), goat anti-rabbit, Alexa Fluor 568 (1:200, ThermoFisher Scientific, A-11036). Figure S1C: rabbit anti-GABA (1:200, Sigma, A2052), goat anti-rabbit, Alexa Fluor 568 (1:200, ThermoFisher Scientific, A-11036), chicken anti-GFP (1:1000, abcam, 13970), goat anti-chicken, Alexa Fluor 488 (1:1000, abcam, 150169). Figures 3A-3E, 5, S2, S4D, and S4E: chicken anti-GFP (1:1000, abcam, 13970), rabbit anti-DsRed (1:200, Takara, 632496), mouse anti-brp (1:10, Developmental Studies Hybridoma Bank (DSHB), nc82), goat anti-chicken, Alexa Fluor 488 (1:1000, abcam, 150169), goat anti-rabbit, Alexa Fluor 568 (1:200, ThermoFisher Scientific, A-11036), goat anti-mouse, Alexa Fluor 647 (1:200, ThermoFisher Scientific, A-21236). Figures S4A and S4C: chicken anti-GFP (1:1000, abcam, 13970), mouse anti-brp (1:10, DSHB, nc82), goat anti-chicken, Alexa Fluor 488 (1:1000, abcam, 150169), goat anti-mouse, Alexa Fluor 647 (1:200, ThermoFisher Scientific, A-21236).

Images were acquired with an LSM700 confocal microscope using 40x oil immersion lenses (NA 1.3). Z stacks were acquired at 1-2 μm intervals between optical sections. Acquired images are visualized and processed offline using Fiji. Montages in the Figure S3 are composed of 6 slices with 5 μm spacing.

MultiColorFlpOut experiments (Figures S4A′, S4B′, and S4C′) were performed as described previously (Xu et al., 2018). Briefly, T2/T3 split-Gal4s were crossed to the MCFO-1 line. Flies were raised at 25°C and heat-shocked at 37°C for 10-20 minutes at mid-pupal stage. Eclosed flies were dissected within two days. Brains were stained following MCFO immunohistochemistry protocol (Nern et al., 2015). Primary and secondary antibodies were used with the indicated concentrations: mouse-anti-Brp (1:20, DSHB, nc82), rabbit anti-HA (1:300, Cell Signaling Technologies, 3724S), rat anti-FLAG (1:200, Novus Biologicals, NBP1-06712), mouse anti-DyLight549-conjugated V5 (1:300, AbD Serotec, MCA1360D549), Alexa Fluor 488 donkey anti-mouse (1:500, Jackson Immuno Research Lab, 715-545-151), Alexa Fluor 647 donkey anti-rat (1:500, Jackson Immuno

Research Lab, 712-605-153), Alexa Fluor 594 donkey anti-rabbit (1:500, Jackson Immuno Research Lab, 711-585-152).

QUANTIFICATION AND STATISTICAL ANALYSIS

Data Analysis—Data were analyzed offline using custom written MATLAB scripts. Images were corrected for motion artifacts using a previously described algorithm (Akin and Zipursky, 2016). To analyze calcium activity in LC11 terminals, a mask was defined encircling LC11 glomerulus. For every pixel in this mask, mean and standard deviation was calculated for the full time series. A test value for each pixel was calculated by the product of mean and standard deviation of each pixel. Pixels with test values greater than or equal to twice the mean value of all test values in the mask were used for analysis. In our experience, this led to the identification of active pixels with good baseline fluorescence and exhibiting strong activity. The frame-wide average of active pixels was used to calculate $\Delta F/F$ time series traces. The calculated time series were filtered with a 2^{nd} order Savitzky-Golay filter with a time span of 150 ms. Traces across multiple trials for the same visual stimulus were averaged for each fly to generate a mean trace.

The following steps were used to analyze data from T cells: For each azimuth position, the total activity across all of the small-field motion stimuli trials (dark object; bright object; short OFF edge; short ON edge) was found. This allowed up to 8 non-overlapping ROIs to be drawn automatically around groups of cells whose receptive fields approximately matched one of the 8 stimulus azimuth positions. We then used the receptive-field locations to shift the time-series of each ROI's responses so that across all ROIs responses approximately aligned in time and could be pooled for averaging. Where multiple elevations were used for horizontal-motion stimuli, we found the elevation which gave the maximum response for each ROI and excluded the data from the other elevations.

Statistics—All statistical tests were performed with the MATLAB Statistics and Machine Learning toolbox (MathWorks, Natick MA). Details of statistical tests used can be found in the figure legends. Nonparametric tests were used.

DATA AND CODE AVAILABILITY

The datasets and MATLAB code supporting the current study have not been deposited in a public repository because accessing these require some training and familiarity with the custom scripting syntax, but are available from the corresponding author on request.

Supplementary Material

Refer to Web version on PubMed Central for supplementary material.

ACKNOWLEDGMENTS

We thank V. Hartenstein for confocal microscope use, M. Reiser, H. Bellen, and G. Card for fly stocks, and M. Wu for providing lab space and equipment to assemble Figure S4. This work was supported by the National Institutes of Health (R01-EY026031 to M.A.F.).

REFERENCES

Ache JM, Polsky J, Alghailani S, Parekh R, Breads P, Peek MY, Bock DD, von Reyn CR, and Card GM (2019). Neural Basis for Looming Size and Velocity Encoding in the Drosophila Giant Fiber Escape Pathway. Curr. Biol 29, 1073–1081. [PubMed: 30827912]

Akin O, and Zipursky SLL (2016). Frazzled promotes growth cone attachment at the source of a Netrin gradient in the *Drosophila* visual system. eLife 5, 961–972.

Apitz H, and Salecker I (2018). Spatio-temporal relays control layer identity of direction-selective neuron subtypes in Drosophila. Nat. Commun 9, 2295. [PubMed: 29895891]

Aptekar JW, Keleş MF, Lu PM, Zolotova NM, and Frye MA (2015). Neurons forming optic glomeruli compute figure-ground discriminations in Drosophila. J. Neurosci 35, 7587–7599. [PubMed: 25972183]

Bennett C, Gale SD, Garrett ME, Newton ML, Callaway EM, Murphy GJ, and Olsen SR (2019). Higher-Order Thalamic Circuits Channel Parallel Streams of Visual Information in Mice. Neuron 102, 477–492. [PubMed: 30850257]

Brand AH, and Perrimon N (1993). Targeted gene expression as a means of altering cell fates and generating dominant phenotypes. Development 118, 401–415. [PubMed: 8223268]

Busch C, Borst A, and Mauss AS (2018). Bi-directional Control of Walking Behavior by Horizontal Optic Flow Sensors. Curr. Biol 28, 4037–4045. [PubMed: 30528583]

Davis FP, Nern A, Picard S, Reiser MB, Rubin GM, Eddy SR, and Henry GL (2018). A Genetic, Genomic, and Computational Resource for Exploring Neural Circuit Function. bioRxiv. 10.1101/385476.

Diao F, Ironfield H, Luan H, Diao F, Shropshire WC, Ewer J, Marr E, Potter CJ, Landgraf M, and White BH (2015). Plug-and-play genetic access to Drosophila cell types using exchangeable exon cassettes. Cell Rep. 10, 1410–1421. [PubMed: 25732830]

Dionne H, Hibbard KL, Cavallaro A, Kao J-C, and Rubin GM (2018). Genetic Reagents for Making Split-GAL4 Lines in *Drosophila*. Genetics 209, 31–35. [PubMed: 29535151]

Douglass JK, and Strausfeld NJ (2003). Retinotopic pathways providing motion-selective information to the lobula from peripheral elementary motion-detecting circuits. J. Comp. Neurol 457, 326–344. [PubMed: 12561074]

Fischbach KF-F, and Dittrich APM (1989). The optic lobe of Drosophila melanogaster. I. A Golgi analysis of wild-type structure. Cell Tissue Res. 258, 441–475.

Fisher YE, Silies M, and Clandinin TR (2015). Orientation Selectivity Sharpens Motion Detection in Drosophila. Neuron 88, 390–402. [PubMed: 26456048]

Fisher YE, Yang HH, Isaacman-Beck J, Xie M, Gohl DM, and Clandinin TR (2017). FlpStop, a tool for conditional gene control in *Drosophila*. eLife 6, e22279. [PubMed: 28211790]

Gale SD, and Murphy GJ (2016). Active Dendritic Properties and Local Inhibitory Input Enable Selectivity for Object Motion in Mouse Superior Colliculus Neurons. J. Neurosci 36, 9111–9123. [PubMed: 27581453]

Haider B, Häusser M, and Carandini M (2013). Inhibition dominates sensory responses in the awake cortex. Nature 493, 97–100. [PubMed: 23172139]

Jenett A, Rubin GM, Ngo TTB, Shepherd D, Murphy C, Dionne H, Pfeiffer BD, Cavallaro A, Hall D, Jeter J, et al. (2012). A GAL4-driver line resource for Drosophila neurobiology. Cell Rep. 2, 991–1001. [PubMed: 23063364]

Keleş MF, and Frye MA (2017a). Object-Detecting Neurons in Drosophila. Curr. Biol 27, 680–687. [PubMed: 28190726]

Keleş M, and Frye MA. (2017b). The eyes have it. eLife 6, e24896. [PubMed: 28165325]

Kim T, and Kerschensteiner D (2017). Inhibitory Control of Feature Selectivity in an Object Motion Sensitive Circuit of the Retina. Cell Rep. 19, 1343–1350. [PubMed: 28514655]

Kim T, Soto F, and Kerschensteiner D (2015). An excitatory amacrine cell detects object motion and provides feature-selective input to ganglion cells in the mouse retina. eLife 4, E2391–E2398.

Lai S-L, and Lee T (2006). Genetic mosaic with dual binary transcriptional systems in Drosophila. Nat. Neurosci. 9, 703–709. [PubMed: 16582903]

Luan H, Peabody NC, Vinson CR, and White BH (2006). Refined spatial manipulation of neuronal function by combinatorial restriction of transgene expression. Neuron 52, 425–436. [PubMed: 17088209]

Maisak MS, Haag J, Ammer G, Serbe E, Meier M, Leonhardt A, Schilling T, Bahl A, Rubin GM, Nern A, et al. (2013).A directional tuning map of Drosophila elementary motion detectors. Nature 500, 212–216. [PubMed: 23925246]

Mauss AS, Vlasits A, Borst A, and Feller M (2017). Visual Circuits for Direction Selectivity. Annu. Rev. Neurosci 40, 211–230. [PubMed: 28418757]

Nern A, Pfeiffer BD, and Rubin GM (2015). Optimized tools for multicolor stochastic labeling reveal diverse stereotyped cell arrangements in the fly visual system. Proc. Natl. Acad. Sci. USA 112, E2967–E2976. [PubMed: 25964354]

Otsuna H, and Ito K (2006). Systematic analysis of the visual projection neurons of Drosophila melanogaster. I. Lobula-specific pathways. J. Comp. Neurol 497, 928–958. [PubMed: 16802334]

Pfeiffer BD, Truman JW, and Rubin GM (2012). Using translational enhancers to increase transgene expression in Drosophila. Proc. Natl. Acad. Sci. USA 109, 6626–6631. [PubMed: 22493255]

Ribeiro IMA, Drews M, Bahl A, Machacek C, Borst A, and Dickson BJ (2018). Visual Projection Neurons Mediating Directed Courtship in Drosophila. Cell 174, 607–621.e18. [PubMed: 30033367]

Shinomiya K, Karuppudurai T, Lin TY, Lu Z, Lee CH, and Meinertzhagen IA (2014). Candidate neural substrates for off-edge motion detection in Drosophila. Curr. Biol 24, 1062–1070. [PubMed: 24768048]

Shinomiya K, Huang G, Lu Z, Parag T, Xu CS, Aniceto R, Ansari N, Cheatham N, Lauchie S, Neace E, et al. (2019). Comparisons between the ON- and OFF-edge motion pathways in the *Drosophila* brain. eLife 8, e40025. [PubMed: 30624205]

Strother JA, Wu ST, Wong AM, Nern A, Rogers EM, Le JQ, Rubin GM, and Reiser MB (2017). The Emergence of Directional Selectivity in the Visual Motion Pathway of Drosophila. Neuron 94, 168–182.e10. [PubMed: 28384470]

Takemura S-Y, Bharioke A, Lu Z, Nern A, Vitaladevuni S, Rivlin PK, Katz WT, Olbris DJ, Plaza SM, Winston P, et al. (2013). A visual motion detection circuit suggested by Drosophila connectomics. Nature 500, 175–181. [PubMed: 23925240]

Takemura S-Y, Xu CS, Lu Z, Rivlin PK, Parag T, Olbris DJ, Plaza S, Zhao T, Katz WT, Umayam L, et al. (2015). Synaptic circuits and their variations within different columns in the visual system of Drosophila. Proc. Natl. Acad. Sci. USA 112, 13711–13716. [PubMed: 26483464]

Takemura S-Y, Nern A, Chklovskii DB, Scheffer LK, Rubin GM, and Meinertzhagen IA (2017). The comprehensive connectome of a neural substrate for 'ON' motion detection in *Drosophila*. eLife 6, e24394. [PubMed: 28432786]

Talay M, Richman EB, Snell NJ, Hartmann GG, Fisher JD, Sorkaç A, Santoyo JF, Chou-Freed C, Nair N, Johnson M, et al. (2017).Transsynaptic Mapping of Second-Order Taste Neurons in Flies by trans-Tango. Neuron 96, 783–795.e4. [PubMed: 29107518]

Tirian L, and Dickson BJ (2017). The VT GAL4, LexA, and split-GAL4 driver line collections for targeted expression in the Drosophila nervous system. bioRxiv. 10.1101/198648.

von Reyn CR, Nern A, Williamson WR, Breads P, Wu M, Namiki S, and Card GM (2017). Feature Integration Drives Probabilistic Behavior in the Drosophila Escape Response. Neuron 94, 1190–1204.e6. [PubMed: 28641115]

Wang H, Dewell RB, Zhu Y, and Gabbiani F (2018). Feedforward Inhibition Conveys Time-Varying Stimulus Information in a Collision Detection Circuit. Curr. Biol 28, 1509–1521.e3. [PubMed: 29754904]

Weir PT, and Dickinson MH (2015). Functional divisions for visual processing in the central brain of flying Drosophila. Proc. Natl. Acad. Sci. USA 112, E5523–E5532. [PubMed: 26324910]

Wiederman SD, Shoemaker PA, and O'Carroll DC (2008).A model for the detection of moving targets in visual clutter inspired by insect physiology. PLoS ONE 3, e2784. [PubMed: 18665213]

Wiederman SD, Shoemaker PA, and O'Carroll DC (2013). Correlation between OFF and ON channels underlies dark target selectivity in an insect visual system. J. Neurosci 33, 13225–13232. [PubMed: 23926274]

Wu M, Nern A, Williamson WR, Morimoto MM, Reiser MB, Card GM, and Rubin GM (2016). Visual projection neurons in the *Drosophila* lobula link feature detection to distinct behavioral programs. eLife 5, e21022. [PubMed: 28029094]

Xu S, Xiao Q, Cosmanescu F, Sergeeva AP, Yoo J, Lin Y, Katsamba PS, Ahlsen G, Kaufman J, Linaval NT, et al. (2018). Interactions between the Ig-Superfamily Proteins DIP-α and Dpr6/10 Regulate Assembly of Neural Circuits. Neuron 100, 1369–1384.e6. [PubMed: 30467079]

Zhang HG, Lee HJ, Rocheleau T, ffrench-Constant RH, and Jackson MB (1995). Subunit composition determines picrotoxin and bicuculline sensitivity of Drosophila gamma-aminobutyric acid receptors. Mol. Pharmacol 48, 835–840. [PubMed: 7476913]

Zhang Y, Kim I-J, Sanes JR, and Meister M (2012). The most numerous ganglion cell type of the mouse retina is a selective feature detector. Proc. Natl. Acad. Sci. USA 109, E2391–E2398. [PubMed: 22891316]

Zhang X, Liu H, Lei Z, Wu Z, and Guo A (2013). Lobula-specific visual projection neurons are involved in perception of motion-defined second-order motion in Drosophila. J. Exp. Biol 216, 524–534. [PubMed: 23077158]

Highlights

- LC11 neurons are suppressed by motion and flicker in the local surround
- LC11 expresses a GABA receptor required for normal object detection
- T2/T3 respond to ON and OFF components of object motion and flicker
- T3 neurons excite LC11 and are required for normal LC11 function

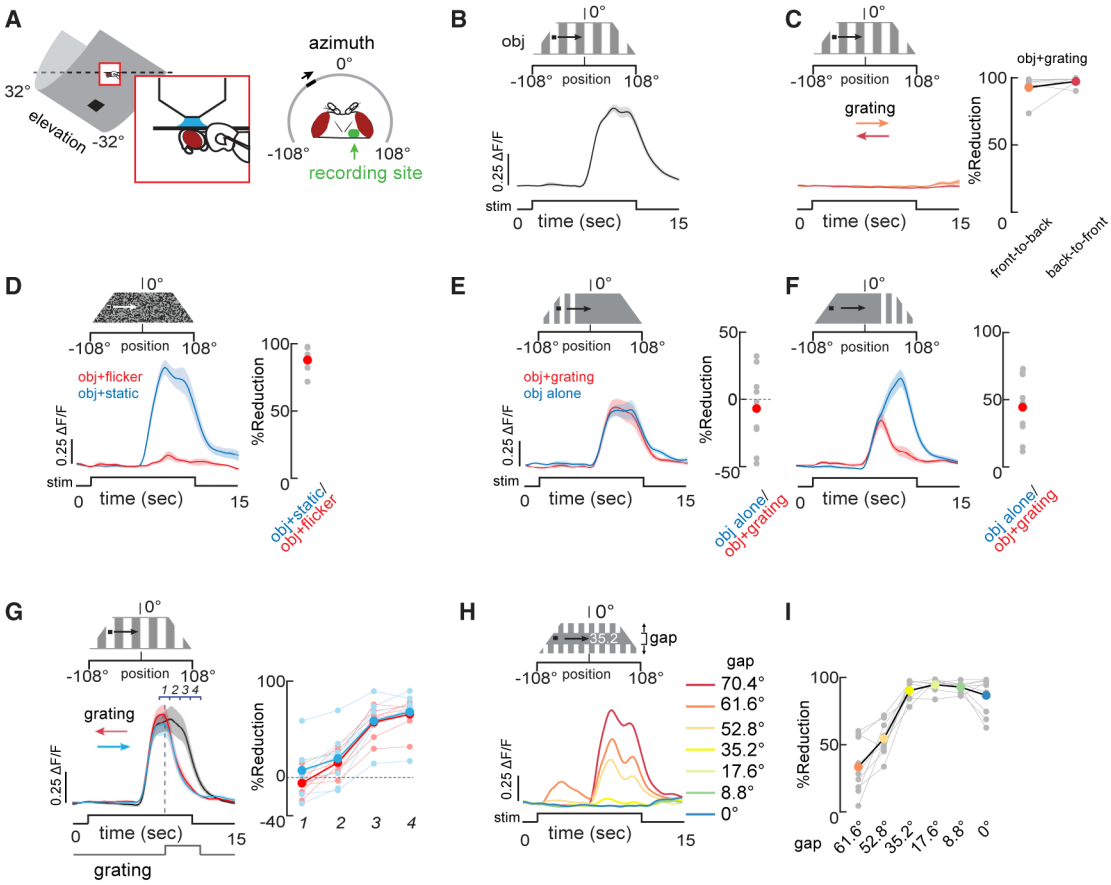

Figure 1. Background Motion or Flicker Suppress Object Responses in LC11

(A) Recording setup: two-photon imaging of GCaMP and LED display for visual stimuli.

(B and C) An 8.8 × 8.8° dark object was moved at 22°/s across the display in the direction shown. A low contrast grating was displayed behind the dark object and was either stationary (B, black trace) or moved horizontally in either direction at 22°/s (C, red, orange traces). n = 8 flies. Reduction in maximum amplitude compared to the stationary background is shown for individual animals (right, gray dots; colored dots indicate the mean across animals).

(D) Each 2.2° pixel on the LED display was flickered at 10 Hz at random (red trace) or was static (blue trace) behind the dark object as it moved across the display. n = 6, shading shows SEM. Reduction in maximum response amplitude when the background was flickered. Red dot shows the mean.

(E and F) Same as (C) except that the grating was displayed only on ¼ of the display screen and either on the contralateral side (E) or ipsilateral side (F). The grating was either stationary (blue trace) or moving (red trace). n = 9. Reduction in maximum response amplitude when the square-wave grating was moving.

(G) Same as (C) except that grating motion onset was delayed until the vertical dashed line. Grating direction indicated by arrows. Reduction in maximum amplitude in the shown epochs 1–4. n = 8.

(H) The grating is displayed on the upper and lower edges of the display and parameterized for the size of the open gap in the object path. The largest gap corresponds to the largest LC11 response. SEM shading is omitted for clarity. n = 9.

(I) Reduction in maximum response amplitude across varying open gaps along the object path. Colored dots correspond to the indicated gaps in (G).

Shading around mean traces indicate SEM. Gray dots indicate individual animals. Red dots in right side panels indicate the mean reduction in maximum amplitude.

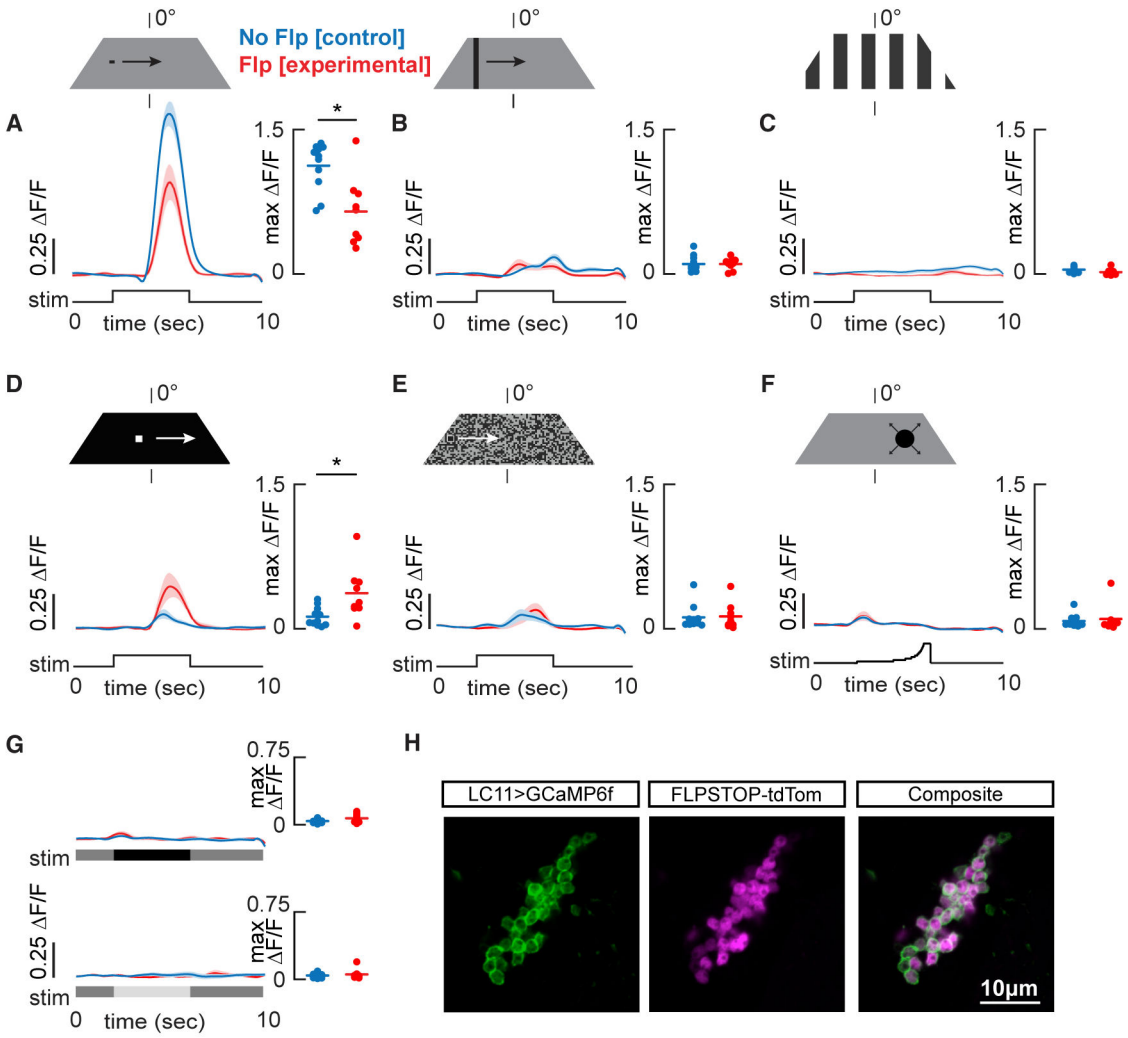

Figure 2. GABA-A Receptor Subunit, *Rdl*, Modulates the Visual Response

(A) LC11 responses to an 8.8° × 4.4° small dark object. Experimental (Flp-mediated inversion of *Rdl*-FLPSTOP cassette) responses is in red. Controls without FLP source in blue. Maximum amplitude of the responses to a small dark object in experimental (red) and control flies (blue).

(B–G) LC11 responses to the following stimuli. (B) 8.8° × 70.6° bar. (C) Square-wave grating. (D) Small bright object. (E) Small dark object moving on a flickering background. (F) Dark looming object. (G) Upper panel: a small stationary dark object. Lower panel: bright object. n = 9 for experimental (Flp) flies (red), n = 11 for control no Flp flies (blue). Dots indicate individual animals. *p < 0.05 Wilcoxon rank-sum test. Shading shows SEM.

(H) Confocal images of LC11 cell bodies stained for GCaMP6f (anti-GFP, green) and tdTomato (anti-DsRed, magenta). Cells that undergone successful FLPSTOP cassette inversion have overlapping GCaMP6f and tdTomato staining.

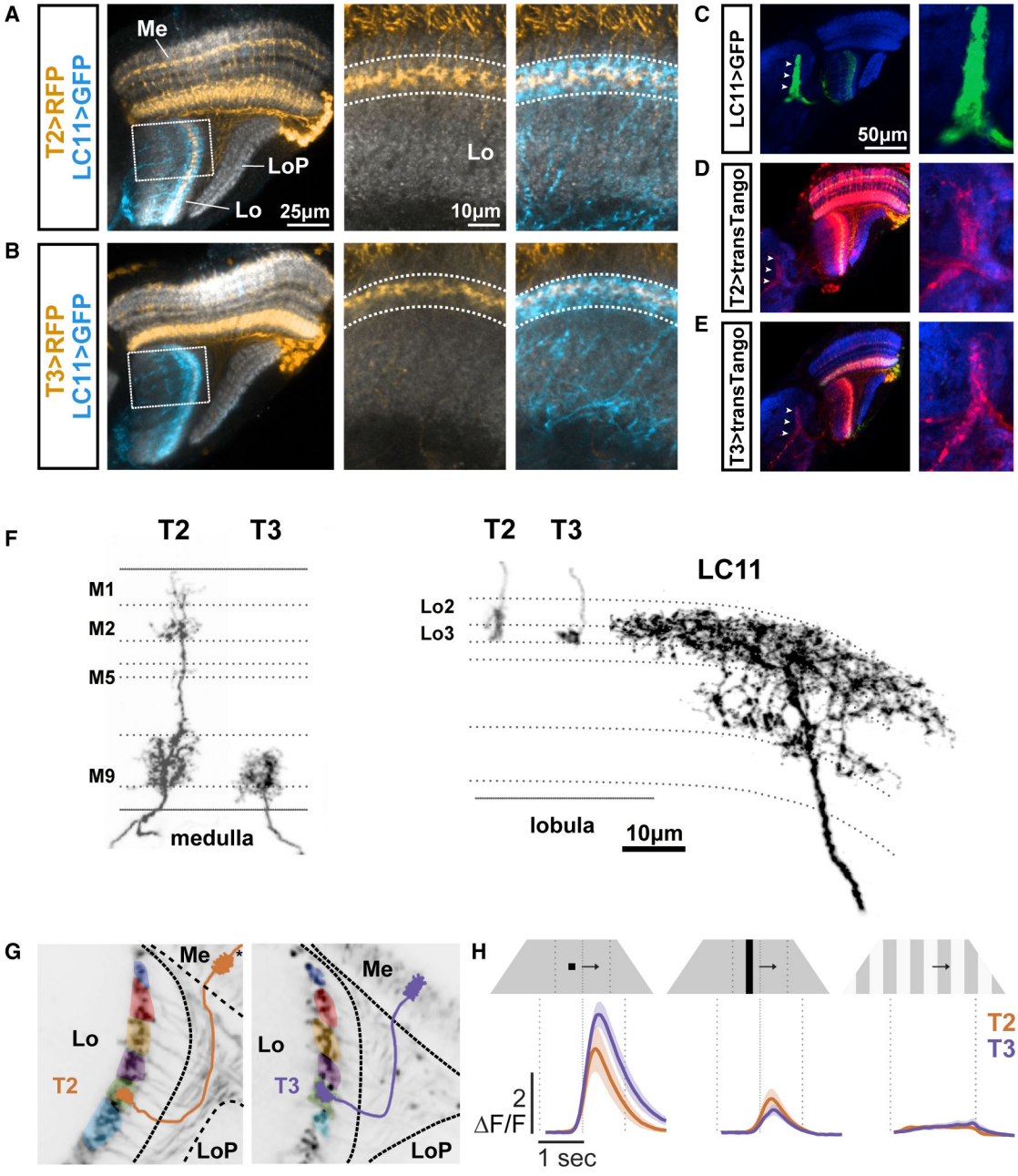

Figure 3. T2 and T3 Are Putative Presynaptic Partners of LC11 and Are Tuned to Small Objects

(A) Dorsal view of T2 neurons (yellow) and LC11 (blue). Right panels: insets from the dashed rectangles with just T2 neurons or T2 with LC11. In each panel, the LC11 dendritic layer is outlined in dashed white line. Neuropil is stained with anti-brp (gray). Lo, lobula; LoP, lobula plate; Me, medulla.

(B) Same as (A) for T3.

(C–E) The glomerular structure of LC11 axon terminals (green) are seen in the dorsal view of the protocerebrum (C, left panel). Anterograde synaptic labeling reagent *trans*-Tango expressed by either T2 (D) or T3 (E) labels LC11 glomerulus in protocerebrum (arrowheads). (D) Putative postsynaptic cells for T2 (green) labeled in red and neuropil is

stained with anti-brp (blue). (E) Same as (D) for T3. (F) Morphologies of individual T2, T3, and LC11 neurons, labeled by MCFO, showing innervation of layers in medulla (left panel) and in lobula (right panel).

(G) Mean activity images from two-photon calcium imaging experiments with GCaMP6f expressed in T2 (left) and T3 (right). Overlaid color patches indicate individual ROIs drawn around terminals in the lobula which responded to a visual stimulus presented at one of eight horizontal positions. Cartoons of individual cells show the projections of T2 and T3 from the medulla to the lobula. Left: Asterisk indicates that the T2 cartoon is incomplete in the medulla, where the distal dendrites are outside of the frame (see Figure 3F)

(H) Mean T2 (brown trace) and T3 (purple trace) GCaMP6f responses to a small dark object, bar and square-wave gratings. n = 6 for T2 and n = 5 for T3. Shading is SEM.

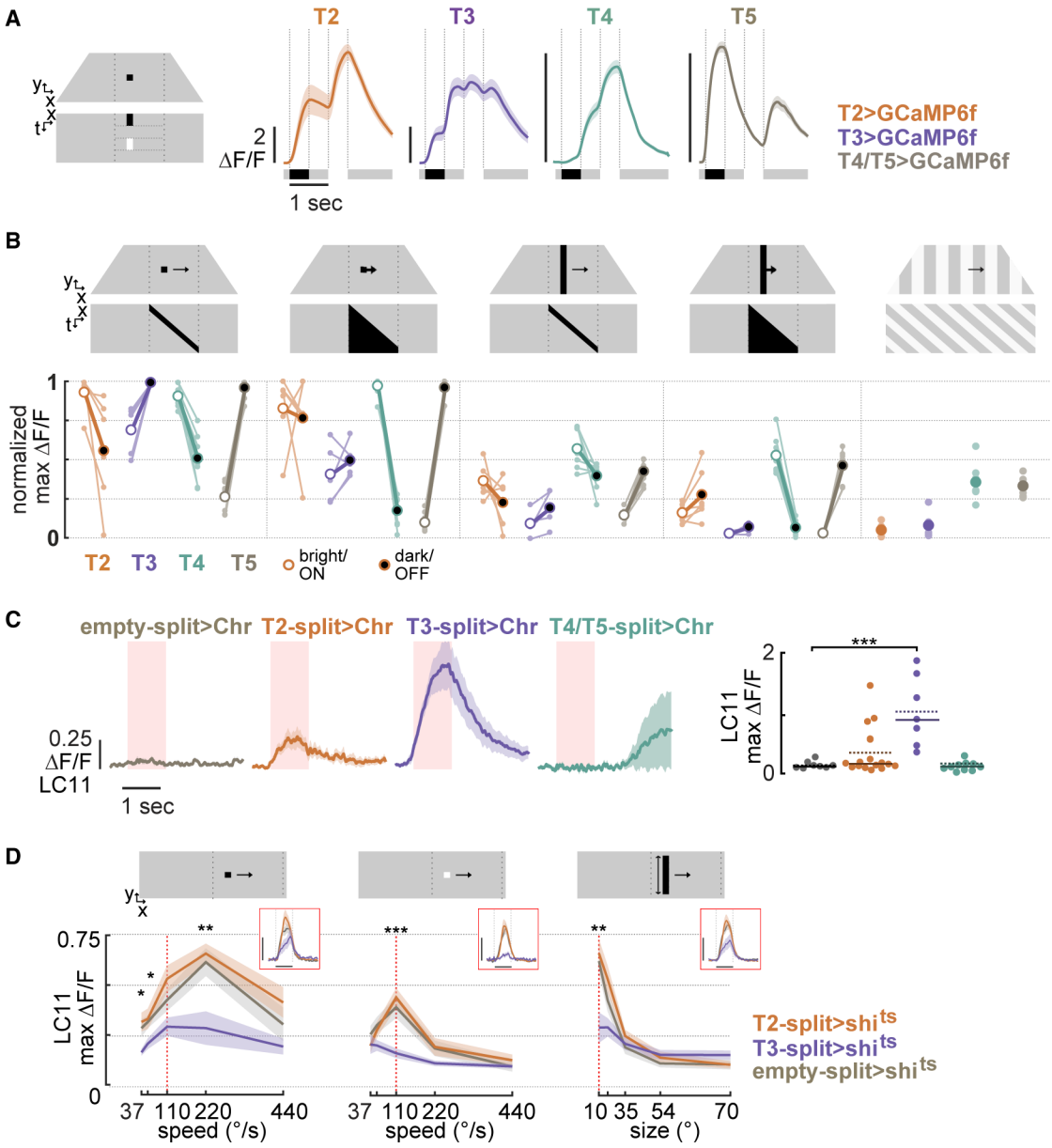

Figure 4. Visual Response Properties of T2 and T3 Columnar Neurons

(A) An 8.8° square object was flashed in place through a sequence that started and ended with the mid-level background intensity and included increments and decrements in brightness as depicted in the pictogram. ROIs were selected from the axon terminals of T2 and T3 terminals in the lobula (see STAR Methods). Results were compared to similar sized ROIs from T4 and T5 dendrites. n = 6 for T2, n = 5 for T3, and n = 8 for T4/T5.

(B) Maximum amplitude responses to each stimulus class is shown for 4 cell types. Each stimulus is represented as a pictogram and space-time trajectories are shown below. Maximum amplitude responses are paired for bright (empty circles) and dark (filled circles) stimuli, and averaged across trials for each individual, shown as connected points for each individual fly. Population mean shown with larger points. Grating response compared to

greatest small object response for each cell, T2: −88%, $p < 0.0001$; T3: −91%, $p < 0.0001$; T4: −55%, $p < 0.0001$; T5: −63% $p < 0.001$ Wilcoxon rank-sum. n = 5.
(C) LC11 activity in response to Chrimson activation of empty-split (gray), T2-split (brown), T3-split (purple), and T4/T5-split (green) (mean ± SEM). The red patch indicates when the Chrimson LED was on. Right: maximum amplitude of each individual's average LC11 response. Horizontal line is median, dashed line is mean. n = 12 for T2, n = 7 for T3, n = 10 for T4/T5, and n = 8 for empty-split flies. ***$p < 0.001$ Wilcoxon rank-sum test.
(D) Size- and speed-tuning of LC11 with blocked synaptic output of T2 (brown) or T3 (purple). Upper: pictograms of the stimulus used for each tuning: a small dark object moving at different speeds, a small bright object moving at different speeds, and a dark object with different vertical sizes moving at 110°/s. Lower: mean maximum amplitude of LC11 activity (+/−SEM) at each speed or size. Insets show mean (+/−SEM) time-series of LC11 activity for the speed or size indicated by the vertical red dashed lines. Horizontal scale bars indicate 1 s of time and vertical scale bars indicate 0.25 ΔF/F. Data from control animals is shown in gray. *$p < 0.05$, **$p < 0.01$, ***$p < 0.001$ Wilcoxon rank-sum test. T3 and control data. n = 9 for T2, n = 9 for T3, and n = 10 for empty-split.

KEY RESOURCES TABLE

REAGENT or RESOURCE	SOURCE	IDENTIFIER
Antibodies		
anti-GFP rabbit polyclonal antibody	ThermoFisher Scientific	A-11122, RRID:AB_221569
anti-brp mouse monoclonal antibody	Developmental Studies Hybridoma Bank	nc82, RRID:AB_2314866
anti-DsRed rabbit polyclonal antibody	Takara	Cat # 632496; RRID:AB_10013483
anti-GFP chicken polyclonal antibody	abcam	Cat# ab13970; RRID:AB_300798
anti-HA rabbit monoclonal antibody	Cell Signaling Technologies	Cat# 3724S; RRID:AB_1549585
anti-FLAG rat monoclonal antibody	Novus Biologicals	Cat# NBP1-06712; RRID: AB_1625981
anti-DyLight549-conjugated V5 mouse monoclonal antibody	AbD Serotec	Cat# MCA1360D549; RRID:AB_915420
Alexa Fluor 488, donkey anti-mouse	Jackson Immuno Research Lab	Cat# 715-545-151; RRID: AB_2341099
Alexa Fluor 488, goat anti-chicken	abcam	Cat# ab150169; RRID:AB_2636803
Alexa Fluor 488, goat anti-rabbit	ThermoFisher Scientific	Cat# A-11008; RRID:AB_143165
Alexa Fluor 647, goat anti-mouse	ThermoFisher Scientific	Cat# A-21236; RRID:AB_141725
Alexa Fluor 647, donkey anti-rat	Jackson Immuno Research Lab	Cat# 712-605-153; RRID: AB_2340694
Alexa Fluor 568, goat anti-mouse	ThermoFisher Scientific	Cat# A-11004 RRID:AB_141371
Alexa Fluor 568, goat anti-rabbit	ThermoFisher Scientific	Cat# A-11036; RRID:AB_10563566
Alexa Fluor 594, donkey anti-rabbit	Jackson Immuno Research Lab	Cat# 711-585-152; RRID: AB_2340621
anti-GABA rabbit polyclonal antibody	Sigma-Aldrich	Cat# A2052; RRID:AB_477652
Experimental Models: Organisms/Strains		
D. melanogaster: LC11-SplitGal4 [*R22H02-p65.AD(attP40); R20G06-Gal4.DBD(attP2)*]	Bloomington	RRID:BDSC_68362
D. melanogaster: LC11-LexA [*R22H02-LexA(attP40)*]	Bloomington	RRID:BDSC_52699
D. melanogaster: LC11-LexA [*R20G06-LexA(attP40)*]	Bloomington	RRID:BDSC_52571
D. melanogaster: LC11-LexA [*R51F09-LexA(attP40)*]	Bloomington	RRID:BDSC_54884
D. melanogaster: T4/T5-SplitGal4 [*R59E08-p65.AD(attP40); R42F06-Gal4.DBD(attP2)*]	JRC, HHMI, G. Rubin	N/A
D. melanogaster: T2-Gal4 [*R47E02-Gal4(attP2)*]	Bloomington	RRID:BDSC_50309
D. melanogaster: T2-Gal4 [*VT012791-Gal4(attP2)*]	JRC, HHMI, B. Dickson	N/A
D. melanogaster: T2-SplitGal4 [*VT012791-p65ADZp(attP40); R47E02- ZpGDBD(attP2)*]	This Study	N/A
D. melanogaster: T3-SplitGal4 [*VT002055-p65ADZp(attP40); R65B04- ZpGDBD(attP2)*]	This Study	N/A
D. melanogaster: T3-Gal4 [*VT002055-Gal4(attP2)*]	JRC, HHMI, B. Dickson	N/A
D. melanogaster: T3-Gal4 [*VT008463-Gal4(attP2)*]	JRC, HHMI, B. Dickson	N/A
D. melanogaster: empty-split Gal4 [*BPp65ADZp(attP40); BPZpGdbd(attP2)*]	Bloomington	RRID:BDSC_79603
D. melanogaster: T2/T3-Gal4 [*R65B04-Gal4(attP2)*]	Bloomington	RRID:BDSC_39336
D. melanogaster: Tm3-Gal4 [*R13E12-Gal4(attP2)*]	Bloomington	RRID:BDSC_48569

REAGENT or RESOURCE	SOURCE	IDENTIFIER
D. melanogaster: Tm4-Gal4 [*R35H01-Gal4(attP2)*]	Bloomington	RRID:BDSC_49922
D. melanogaster: Tm9-Gal4 [*0137-Gal4*]	Bloomington	RRID:BDSC_62661
D. melanogaster: Tm2-Gal4 [*VT12282-Gal4 (attP2*]	VDRC	203097
D. melanogaster: *13xLexAop2-IVS-GCaMP6f-p10(su(Hw)attP5)*	Bloomington	RRID:BDSC_44277
D. melanogaster: *20xUAS-IVS-GCaMP6f(attP40)*	Bloomington	RRID:BDSC_42747
D. melanogaster: *8xLexAop2-FLPL(attP40)*	Bloomington	RRID:BDSC_55820
D. melanogaster:*10xUAS-IVS-mCD8::RFP(attP18),13LexAop2-IVS-mCD8::GFP(su(Hw)attP8*	Bloomington	RRID:BDSC_32229
D. melanogaster: *UAS-myrGFP.QUAS-mtdTomato-3xHA(su(Hw)attP8); trans-TANGO (attP40)*	Bloomington	RRID:BDSC_77124
D. melanogaster: *Mi{FlpStop}Rdl[MI02620-FlpStop.ND]*	Bloomington	RRID:BDSC_67682
D. melanogaster: *Mi{Trojan-Gal4.1}Rdl[MI02957-TG4.1]*	Bloomington	RRID:BDSC_65421
D. melanogaster: *Mi{Trojan-GAL4.0}nAChRalpha1[MI00453-TG4.0]*	Bloomington	RRID:BDSC_66780
D. melanogaster: *Mi{Trojan-GAL4.2}nAChRalpha5[MI13859-TG4.2]*	Bloomington	RRID:BDSC_76755
D. melanogaster: *Mi{Trojan-GAL4.1}nAChRalpha6[MI01466-TG4.1]*	Bloomington	RRID:BDSC_76137
D. melanogaster: *Mi{Trojan-GAL4.1}nAChRalpha7[MI12545-TG4.1]*	Bloomington	RRID:BDSC_77828
D. melanogaster: *Mi{Trojan-GAL4.0}ChAT[MI04508-TG4.0]*	Bloomington	RRID:BDSC_60317
D. melanogaster: *Mi{Trojan-GAL4.2}VGlut[MI04979-TG4.2]*	Bloomington	RRID:BDSC_60312
D. melanogaster: *pBPhsFlp2::PEST (attP3); pJFRC201-10XUAS-FRT > STOP > FRT-myr::smGFP-HA (VK0005), pJFRC240-10XUAS-FRT > STOP > FRT-myr::smGFP-V5-THS-10XUAS-FRT > STOP > FRT-myr::smGFP-FLAG (su(Hw)attP1)*	Bloomington	RRID:BDSC_64085
D. melanogaster: *10XUAS-Syn21-Chrimson88-tdT-3.1 (attP18)*	JRC, HHMI, M. Reiser, Strother et al., 2017	N/A
D. melanogaster: *LexAop2-Syn21-opGCaMP6s (su(Hw)attP8)*	JRC, HHMI, M. Reiser, Strother et al., 2017	N/A
D. melanogaster: *20XUAS-TTS-Shibire-ts1-p10 (VK0005)*	JRC, HHMI, G. Rubin, Pfeiffer et al., 2012	N/A
Software and Algorithms		
MATLAB R2016a	MathWorks	https://www.mathworks.com/
Affinity Designer	Serif	https://www.serif.com/en-us/
Fiji	http://fiji.sc/	RRID: SCR_002285
Slidebook	https://www.intelligent-imaging.com/slidebook	SlideBook , RRID:SCR_014300